A Verilog-A Model for a Light-Activated Semiconductor Gas Sensor

Juan Luis Soler-Fernández, Olga Casals, Cristian Fàbrega, Hongqiang Li, Angel Diéguez, J. Daniel Prades, and Oscar Alonso

***Abstract*—Light activation is a demonstrated alternative to heating for promoting gas response in semiconductor gas sensors. After two decades of research, the underlying mechanisms behind their responses are still discussed, but experiments have shown consistent trends under different light conditions and gas concentrations. Based on these consolidated qualitative observations, we propose a phenomenological model that predicts quantitatively the resistance changes in light-activated gas sensors, exclusively based on a set of parameters that can be determined in advance, from dedicated experiments. It is a modular Verilog-A model that incorporates effects, such as photoconductivity, dynamic response to gases, irradiance influence on the sensitivity, and baseline drift. We validated the model with experimental data, showing it can predict observations in short and long timescales. We make its source-code fully available to the community, so that it can be used right away to help engineers to design interfaces for this kind of sensors, and it can be modified by peers to incorporate additional refinements.**

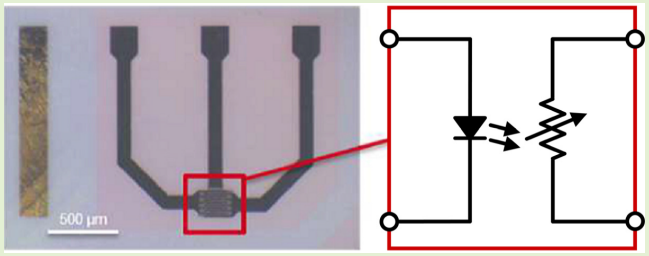

***Index Terms*— Behavioral simulation, gas sensor, light-emitting diode (LED), metal oxide, photograph/light activation, Verilog-A model.**

I. Introduction

AIR pollution and environmental contamination is one of the main problems of today's society. According to the World Health Organization (WHO), it causes more than 6 million premature deaths every year around the world, regardless of the wealth of the country [1]. This reason prompted researchers to study and develop new technologies to monitor and control such hazardous gases, making people aware of how vulnerable we are to the impacts of climate change.

Gas sensors are key components to address this monitoring problem and are present in many industrial and domestic systems for environmental pollution monitoring [2], [3], energy management [4], efficient mobility [5], safety [6], and security [7], [8]. These sensors provide critical information not only about the presence of a certain gas or gases, but also about their concentration in a specific location, allowing individuals and organizations to take appropriate actions to protect human health and safety, prevent accidents and damage, and optimize processes and operations.

To date, several gas sensing technologies emerged using MEMS [9], such as surface acoustic wave (SAW) [10] or fiber optic devices [11], among others [12]. Solid-state semiconductor gas sensors (interrogated in conductometric mode typically made of a semiconductor, such as metal oxides (SMOs) [13], carbonaceous materials [14], or polymers [15]) offer a robust and cost-effective solution. SMO gas sensors are good candidates for mass production in the monitoring of the environment because of their small footprint, high sensitivity, and fast response times. Nevertheless, further improvements in power consumption and improved selectivity are necessary to satisfy today's demands.

In the presence of a specific gas, the conductance from SMO sensors can only either increase or decrease; limiting the amount of information they can provide. To illustrate this,

Manuscript received 19 March 2024; revised 21 May 2024; accepted 25 May 2024. Date of publication 5 June 2024; date of current version 16 July 2024. This work was supported in part by the European Union's Horizon 2020 Research and Innovation Program under Grant 951774 (FOXES). The work of Juan Luis Soler-Fernandez was supported by the Spanish Ministry of Universities through FPU Fellowship under Grant FPU22/01008. The work of J. Daniel Prades was supported in part by the Alexander von Humboldt Professorship of the Humboldt Foundation, and in part by the Federal Ministry for Education and Research, Germany. The associate editor coordinating the review of this article and approving it for publication was Dr. Anuj K. Sharma. *(Corresponding author: Juan Luis Soler-Fernández.)*

Juan Luis Soler-Fernández, Olga Casals, Cristian Fàbrega, Angel Diéguez, and Oscar Alonso are with the Department of Electronics and Biomedical Engineering, Universitat de Barcelona, 08028 Barcelona, Spain (e-mail: j.soler@ub.edu; olga.casals@ub.edu; cfabrega@ub.edu; angel.dieguez@ub.edu; oalonso@ub.edu).

Hongqiang Li is with Tianjin Key Laboratory of Optoelectronic Detection Technology and Systems, School of Electrical and Electronic Engineering, Tiangong University, Tianjin 300387, China (e-mail: lihongqiang@tiangong.edu.cn).

J. Daniel Prades is with the Institute of Semiconductor Technology (IHT), Laboratory for Emerging Nanometrology (LENA), Technische Universität Braunschweig, 38106 Braunschweig, Germany, and also with the Department of Electronics and Biomedical Engineering, Universitat de Barcelona, 08028 Barcelona, Spain (e-mail: daniel.prades@tu-braunschweig.de).

Digital Object Identifier 10.1109/JSEN.2024.3407651

let us consider oxygen as a representative gas. In materials designed for gas sensing, such as SnO_2, ZnO, WO_3, In_2O_3, TiO_2, and so on, which are n-type SMO [16], electrons are the predominant charge carriers. When oxygen ions are adsorbed onto an n-type SMO, they capture electrons from the material, resulting in a decrease in conductance (or an increase in resistance). Conversely, when oxygen ions are desorbed, facilitated by a reaction with a reducing substance, electrons are released into the material's bulk. This process leads to an increase in conductance (or a decrease in resistance). A typical example of this kind of process is the oxidation of carbon monoxide on the surface of metal oxides, leading to the release of carbon dioxides and a free electron ($CO_{[gas]} + O^-_{[ion\ ads]} \rightarrow e^- + CO_{2[gas]}$) [17]. Reciprocally, in p-type materials (such as CuO, NiO, Co_3O_4, Cr_2O_3, and so on) [18], where the majority charges are holes, the signal variations develop in the opposite directions, increasing the conductivity in the presence of an oxidizing gas and decreasing it with a reducing gas [19]. Therefore, an SMO gas sensor can basically distinguish just the oxidizing (e.g., O_2, NO_2, O_3, and so on) or reducing (e.g., CO, NO, NH_3, C_xH_y, alcohols, and so on) character of the target gas, and not strictly its precise composition.

For this reason, research in SMO materials has been devoted during many decades to devise complementary reaction paths, where the fundamental oxidizing/reducing processes can mostly develop in the presence of the gas of interest, to attain some level of gas specificity in the SMO sensors signals. These strategies involved the modification of the basic metal oxide materials with additives, the formulation of multimetallic oxides, or the use of catalytic centers and particles, among many others [20].

Traditionally, heating has been used to operate these devices in thermodynamic conditions that favor the abovementioned oxidation/reduction/catalytic interactions between the semiconductor surfaces and the molecules of the target gas [21]. This implies temperatures of a few hundred Celsius degrees, associated with important power consumption levels, despite miniaturization efforts [22].

As an alternative, light can be used to promote such gas–surface interactions [23], rendering equivalent gas sensing performances [24]. These conductometric SMO sensors working under illumination can be regarded as an impedance varying with the presence of the target gas [25] (that mimics the SMO response) coupled to an electrooptic light emitter, such as an LED (causing the appropriate reaction activation). Fig. 1 shows an equivalent electrical model of this concept, where R_{SENSOR} represents the variable resistance of the SMO material, C_P is the parasitic capacitance of the interconnection, and L_S is the LED light source. This model depends on the many design parameters of the device, such as the SMO material chosen, its crystalline microstructure, surface area and thickness, the contacts layout, the placement, and dimensions of the LED [26].

Typically, the R_S resistance change of the SMO material has a dynamic range of multiple orders of magnitude in response to gases and light, with a base resistance that will also depend on the reproducibility and variations of the fabrication methods (temperature, humidity, and so on). Such variability

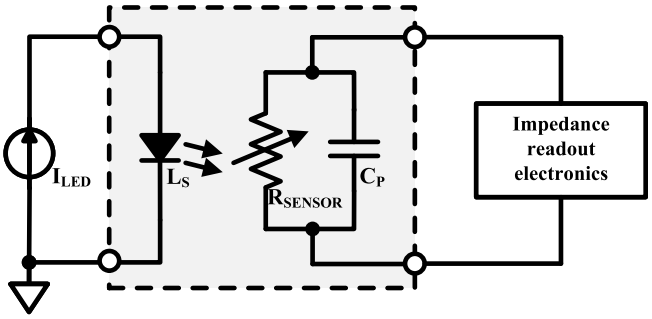

Fig. 1. Equivalent electrical model of an illuminated SMO gas sensor (inside the dotted box).

adds complexity to the readout interface, the signal processing, and calibration methods used. The capacitive component of the impedance (mainly coming from the contacts) can play a key role during the transient measurements and must be considered, especially in time-modulated measurements. The illumination conditions are key to stablish the working conditions of the SMO material and its reactivity. Therefore, accurate means to control the electric bias of the LED, and consequently, the light irradiance levels reaching the SMO material are needed. A better electrical control of the light emission in LEDs typically calls current driving.

To date, illuminated gas sensors have been much less investigated than their heated counterparts, but there exists abundant evidence of their viability either using conventional metal oxides (SnO_2, WO_3, or TiO_2 [27]), carbon nanotubes (CNTs) [28], and other carbonaceous structures (CNF [29] and graphene [30]). Responses to both oxidizing (such as NO_2 or O_3 [31]) and reducing (such as H_2 or CO [32]) species have been demonstrated. Also, light of photon energies above and below the semiconductor bandgap has been used, as well as different intensities, both in steady and time-modulated illumination conditions.

Out of this knowledge, there exist a variety of light-activated sensing mechanisms proposed [33], [34] that mostly share a few phenomenological features.

1) Light lowers the baseline resistance of the sensor, by means of photoconductivity.
2) In the absence of light, response to gases is negligible, but in the excess of light, the response also decays (thus, a sweet spot of irradiance for best response should be found).
3) Light systematically speeds up the response and recovery times, suggesting that it favors both gas adsorption and desorption mechanisms.

Moreover, with light, it is possible to attain dramatic power savings following the usual path of miniaturization combined with energy efficient light sources (such as LEDs) [35]. This opens the door to the use of semiconductor gas sensors even in power limited IoT applications, which is an expanding field aiming to supply the high demand of more interconnected daily devices to ease people's life.

However, a sensor device is only useful integrated in an electronic system of a higher complexity. Therefore, taking advantage at a system level of the theoretical power savings attained at a device level implies developing custom electronic

interfaces capable of meeting sufficient control (i.e., driving the LED), measurement (i.e., measuring the resistance), processing (e.g., signal processing and calibration), and connectivity (e.g., wireless communications range and data rate) performances, with a moderate power budget.

To address this problem, we present here a phenomenological model, capable of predicting the electrical behavior of illuminated sensors under varying illumination and gas conditions. It is solely based on a reduced set of parameters that can be assessed experimentally in advance. This new model will serve researchers to optimize working conditions toward response, dynamics, or power consumption, as well as system engineers to emulate in full the sensor behavior when implementing electronic control, readout electronics, processing, and communication interfaces.

Ours is a behavioral electrical model described in Verilog-A [36], an analog modeling language commonly used in electronic design automation (EDA) tools. The model can be implemented directly into the design software (e.g., Cadence Virtuoso) to simulate the sensor behavior together with its electronic interface. This powerful feature allows the designer to optimize the circuitry to drive and measure the sensor. Since electronics simulations are computational hungry, the model of the sensor must be efficient. In consequence, we avoided to describe the chemical and molecular processes and focused on the behavior of the output response (i.e., resistance) to a given input (i.e., illumination and gas conditions over time), treating the model as a black box that responds closely enough to the real SMO illuminated gas sensors, for system design purposes. The model is defined by a set of parameters that allow the user to easily modify the behavior without modifying the code. For this reason, the model can describe the response to any kind of gas and/or illumination source (e.g., wavelength and intensity), for which the calibration data needed to set up the model are available. To facilitate revision, access, reuse and improvement of the model, we made it available publicly in a GitHub repository.

II. Model Details

In this section, we present a detailed explanation of the model. The complex behavior of the gas sensor is split into the basic contributions presented in the block diagram of Fig. 2, where each block implements mathematically a specific phenomenological aspect of the sensor's behavior.

The model takes as inputs the signal applied to switch on and control the LED brightness, which can be either controlled by a voltage source ($V_{\mathrm{LED}}(t)$) or by a current source ($I_{\mathrm{LED}}(t)$), and the evolution of the gas concentration around the sensor (Gas(t)), both represented by programmable sources. The sensor response to gas blends (accounting for, e.g., interference and selectivity) can be modelized by placing multiple response-model blocks in parallel fed with independent signal sources associated with each one of the gases. Other features of gases, such as the flow speed, can also be introduced through the dynamic properties of voltage source representing the gas. The output, in turn, is the output resistance ($R_{\mathrm{SENSOR}}(t)$) observed between two terminals (R_p and R_n) under a constant probing voltage (V_{REF}). To render

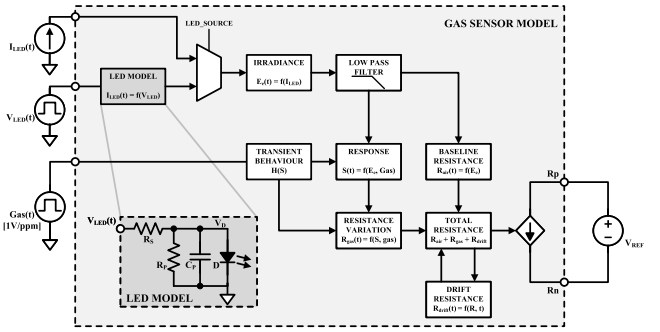

Fig. 2. Block diagram of the photoactivated gas sensor model and equivalent electrical circuit of the LED.

quantitative outputs, the model needs a set of experimental parameters described in the following lines.

We begin modeling the illumination source to evaluate the excitation level of the sensor. The inset in Fig. 2 shows the equivalent electrical circuit of an LED used when voltage is used to control the brightness. The current flowing through the LED (I_{LED}) can be directly obtained in Verilog-A by defining the series resistance (R_S) (modeling the contacts), followed by three parallel branches containing a shunt resistor (R_P), a parallel capacitor (C_P) (modeling the junction leakage and capacitance, respectively), and an ideal diode (D) that follows the electrical behavior

$$I_D(t) = I_S \cdot \left[\exp\left\{(qV_D(t))\big/nkT\right\} - 1\right] \tag{1}$$

where I_S is the inverse saturation current, q is the elementary charge, k is the Boltzmann's constant, n the ideality factor, T represents the absolute temperature, and V_D is the voltage effectively dropping between the ideal diode terminals. This mathematical model is implemented in Verilog-A as follows:

```
  // LED model
  I(vled, vledA) <+ V(vled,vledA) /
LED_RS;
  I(vledA,vss) <+ V(vledA,vss) / LED_RP;
  I(vledA,vss) <+ LED_CP *
ddt[V(vledA,vss)];
  V(iled,vss) <+ I(iled,vss) * 1;
  if(LED_SOURCE)
  led_curr = I(iled,vss);
  else
  led_curr
   = LED_IS *
  exp[`P_Q*V(vledA,vss)/(LED_N*`P_K*$
temperature)];
  I(vledA,vss) <+ led_curr;
```

LED operation under current controlled conditions is usually preferred experimentally. Here, the voltage option was given for simplicity. Due to the ideality of the models, negligible effects due to this difference were observed in the results.

Alternatively, the LED current can be directly fed into the model and selected with a multiplexer in the model. The resulting light irradiance (E_e) impinging on the semiconductor surface [37], [38] follows an almost linear relationship with the electrical input power before it saturates [39] and can be modeled with (2) and then fed into a low-pass filter (LPF) to

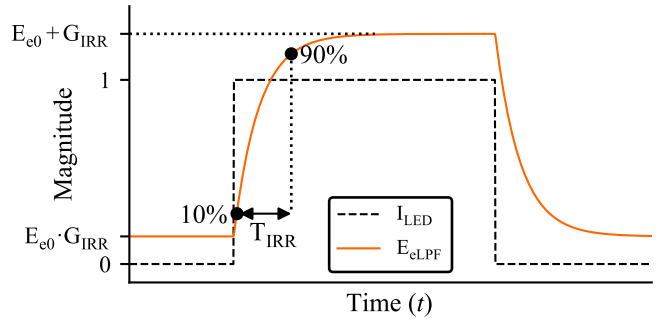

Fig. 3. Irradiance model response to a variation in the LED current.

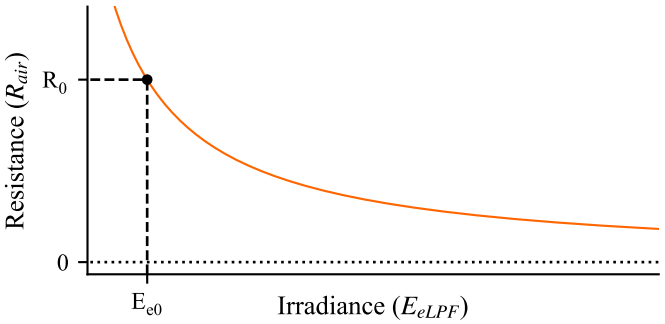

Fig. 4. Semiconductor resistance variation under irradiance.

simulate the dynamic behavior of the semiconductor layer in response to the photoexcitation (3)

$$E_e(t) = E_{e0} + E_{eM} \cdot I_{\text{LED}}(t) \tag{2}$$

$$E_{e\text{LPF}}(s) = E_e \cdot G_{\text{IRR}} / (T_{\text{IRR}} \cdot s + 1) \tag{3}$$

where E_{e0} represents the background irradiance (coming eventually from, e.g., the ambient light) and E_{eM} is the variation of the irradiance with the LED current (I_{LED}). G_{IRR} is a parameter to adjust the irradiance gain if needed, and T_{IRR} is the time constant of the LPF (see Fig. 3). The Verilog-A implementation of this block is shown in the following code, where it can be observed that the filter is actually defined in the Laplace domain through the laplace_nd() function:

```
// Irradiance
irr = IRR_0 + IRR_M*led_curr;
// Irradiance low pass filter
irr_lp = laplace_nd(irr, {IRR_GAIN},
{1,IRR_TP});
```

The first parameter derived from the photoexcitation state (i.e., the irradiance level) is the baseline resistance photoconductance of the sensor exposed to clean air (R_{base}): the resistance drops under optical excitation due to the additional free charges made available in the semiconductor upon photon absorption (see Fig. 4) following a behavior like:

$$R_{\text{base}}(t) = R_0 / \left(1 + \alpha \cdot (E_{e\text{LPF}}(t) - E_{e0})^{\beta}\right) \tag{4}$$

where R_0 is the material resistance under ambient irradiance conditions, and α and β are fitting parameters. The Verilog-A implementation is written as follows:

```
// Light effects on sensor resistance
r_base = SENSOR_R0 / [1 +
RBASE_ALPHA*(irr_lp-IRR_0)**RBASE_BETA].
```

In parallel, to build the sensor response in the time domain, we started with the sequence of gas concentration levels

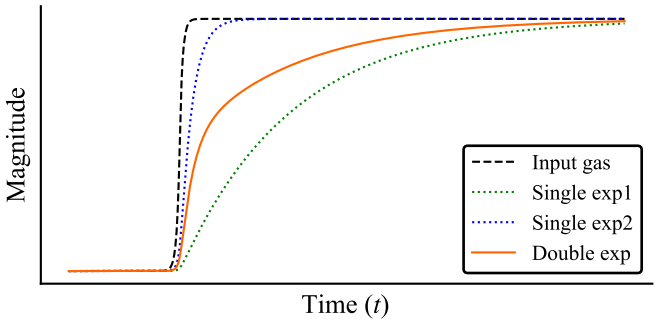

Fig. 5. Representation of the double exponential response.

applied to the gas sensor Gas(t). The sensor output can be regarded as a filtered version of this signal, amplified according to the sensor sensitivity and delayed following the sensor dynamic characteristics. This behavior is emulated by a transfer function $H(s)$ in the form shown in (5). We formulated this transfer function as a combination of two exponential transients (τ_1 and τ_2) (Fig. 5) with a certain gain (A), following the many multiexponential examples in the literature [34]. This operation generates a "filtered" gas concentration signal $\text{Gas}_f(s)$, denoted in (6), that is then used as a basic s-domain template modified in amplitude in the subsequent blocks

$$H(s) = A/2 \cdot \left[1/(\tau_1 s + 1) + 1/(\tau_2 s + 1)\right] \tag{5}$$

$$\text{Gas}_f(s) = H(s) \cdot \text{Gas}(s). \tag{6}$$

An aspect to take into account in the model is that, despite Verilog-A supports S-domain operations, it does not allow a dynamic behavior of the poles and zeros that are observed in the sensor due to different gas concentrations and asymmetric responses. For this reason, the model considers this dynamic output in the form of the time domain differential (7) that corresponds to the transformation of (6). It is worth noting that, to favor the convergence of the simulator between time points, the equation is written in the integral form

$$\text{Gas}_f(t) = \int \left[\int \left(A \cdot \text{Gas}(t) - \frac{\text{Gas}_f(t)}{\tau_1 \tau_2} \right) \cdot dt - \left(\frac{1}{\tau_1} + \frac{1}{\tau_2} \right) \text{Gas}_f(t) \right] \cdot dt \tag{7}$$

where A is the gain of the input, and τ_1 and τ_2 are the two time constants of each exponential transient. This also allows us to characterize the dependence of the settling time to the irradiance and gas concentration. To convert the equation into the integral form, the only step is to solve for $\text{Gas}_f(s)$ in terms of $1/s$.

Following the experimental evidence from [38], the first time constant τ_1 is related to the irradiance as per (8), while the second, τ_2, is independent and is associated with the rate of change of the gas surrounding the sensor (e.g., the gas injection speed of the chamber where the tests of the sensor have been carried out). Equation (9) showcases that this second time constant is directly controlled by a parameter to add some flexibility to the model and accommodate multiexponential deviations

$$\tau_{1\text{ON}}(t) = T_0 \cdot (1/E_e(t))^{T_M} \tag{8}$$

$$\tau_2 = T_2. \tag{9}$$

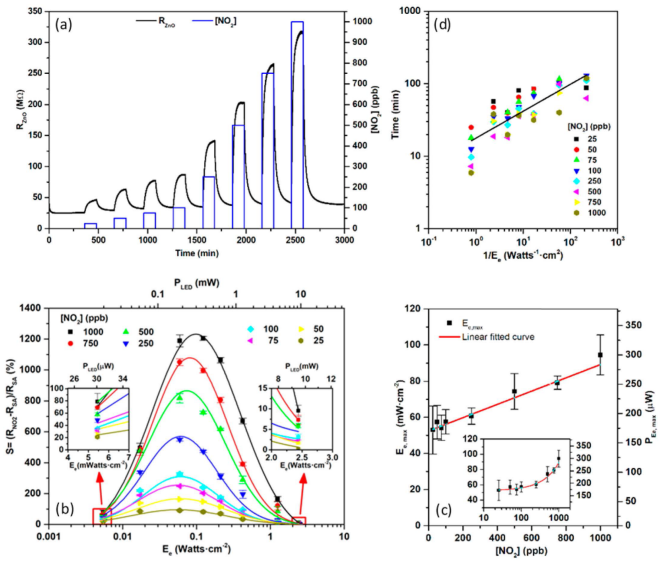

Fig. 6. Examples of the experimental data used to determine the model parameters. (a) Resistance record of the ZnO sensor to increasing concentrations of NO_2. (b) Summary of the responses obtained to NO_2 concentrations ranging from 25 ppb to 1 ppm with increasing irradiance/power levels. (c) Irradiance at which the maximum response is reached, as a function of the NO_2 gas concentration. (d) Summary of the response times (defined as the 10% to 90% of the signal rise time) obtained to NO_2 concentrations ranging from 25 ppb to 1 ppm as a function of the invers irradiance. Reprinted with permission from [38]. Copyright 2024 American Chemical Society.

Comparing the response and recovery processes, it has also been observed that their dynamics are asymmetric [40]. This behavior has been parametrized as a ratio between the response (on) and recovery (off) time constants

$$\tau_{1\mathrm{OFF}}(t) = \tau_{1\mathrm{ON}}(t) \cdot T_{\mathrm{OnOff}}. \tag{10}$$

Notice that in the model, all these time constants evolve with time, due to their dependence with the irradiance [hence, the explicit (t) notation].

Finally, the amplitude of this dynamic track is scaled to the different factors that determine the response magnitude (S): the filtered gas concentration (Gas_f) and the irradiance level (E_e). In this work, we used the following definition for the sensor response to gases:

$$S = \left(R_{\mathrm{gas}} - R_{\mathrm{base}}\right) / R_{\mathrm{base}}. \tag{11}$$

Previous works [38] concluded that while response evolves with irradiance following a complex bell-shape trend [see Fig. 6(b)], the peak of such trend scales linearly with the gas concentration. This interdependency is captured in the model as follows:

$$S_{\max}(t) = S_M \cdot \mathrm{Gas}_f(t) + S_0 \tag{12}$$

$$\mu(t) = \ln\left(S_{\max}(t)\right) + \sigma^2 \tag{13}$$

$$S(t) = \mathrm{Gas}_f(t) \Big/ \left(E_e(t) \cdot \sigma\sqrt{2\pi}\right) \cdot \exp\left\{-\left(\ln\left(E_e(t)\right) - \mu(t)\right)^2 \Big/ \left(2\sigma^2\right)\right\} \tag{14}$$

where S_M and S_0 are linear fitting parameters and σ is the bell width (also a parameter and treated as a constant, although it can slightly vary from bell to bell). All parameters can be extracted from the calibration curves of a given sensor. Also, alternative relationships can be inserted in our model to describe different response behaviors. Observations in light-activated gas sensors showed that the response of the sensing material is highly dependent on the light source wavelength. In this model, the user can model sensors operating at different wavelengths, by gathering appropriate experimental data acquired at that wavelength and setting up the parameters accordingly.

Once stablished the dynamic and magnitude response of the sensor, we translated these effects into actual resistance values (R_{gas}) following

$$R_{\mathrm{gas}}(t) = R_{\mathrm{base}}(t) \cdot S(t). \tag{15}$$

Also, we included in our model resistance drift effects due to their relevance in SMO gas sensors. Independently of the manifold and complex causes (such as chemical diffusion of oxygen species, physical changes of the semiconductor layer, degradation of metal contacts, and so on [41]), we found that a simple linear term over time with a single drift coefficient (C_D) was enough to sufficiently capture these effects in the experimental data available

$$R_{\mathrm{drift}}(t) = C_D \cdot t. \tag{16}$$

Again, other laws to depict more complex drift behaviors or a better understating of the underlying mechanisms can be incorporated in future refinements.

Finally, the sensor resistance value observed experimentally $(R_{\mathrm{SENSOR}}(t))$ is the aggregate of all abovementioned terms

$$R_{\mathrm{SENSOR}}(t) = R_{\mathrm{base}}(t) + R_{\mathrm{gas}}(t) + R_{\mathrm{drift}}(t). \tag{17}$$

A. Summary of Model Parameters

The model behavior is fully defined by the set of parameters summarized in Table I following the order in which they are presented in this article. The column "symbol" shows the notation used in the equations of this article, while the column "parameter" provides for clarity the plain-text notation used in the Verilog-A code.

III. Experimental Details

A. Reference Measurements

To validate our model, we compared the predictions of the simulations with experimental measurements from samples of illuminated gas sensors published elsewhere [38] (Fig. 6).

These devices are built around a miniaturized LED (micro-light plate configuration—μLP), where the SMO material (ZnO nanoparticles) is placed directly on top of the planar μLP LED structure, only separated by a few hundred nanometers to insulate it electrically. Consequently, almost all the light emitted by the LED impinges on the sensor SMO, allowing for very well-controlled, uniform, and high irradiances levels, with a reduced electrical power consumption. The μLP exposes four independent pads: two to operate the blue InGaN LED (455-nm peak emission) and two more to measure the electrical resistance of the SMO material lying across a pair of interdigitated electrodes. These sensors performed particularly well detecting NO_2, ranging from a few parts per billion (ppb)

TABLE I
MODEL PARAMETERS DESCRIPTION

Symbol	Parameter	Description
–	MC_N	Number of Montecarlo iterations. If 1: no MC is applied. If 2: maximum corner is applied. If 3: minimum corner is applied
–	MC_SEED	Montecarlo seed
–	LED_SOURCE	LED excitation source. If 0: voltage driven. If 1: current driven
R_S	LED_RS	LED series resistance
R_P	LED_RP	LED parallel resistance
C_P	LED_CP	LED parallel capacitance
I_S	LED_IS	LED reverse saturation current
n	LED_N	LED ideality factor
T_{IRR}	IRR_TP	Irradiance LPF pole (time constant)
G_{IRR}	IRR_GAIN	Irradiance gain
E_{e0}	IRR_0	Ambient irradiance
E_{eM}	IRR_M	Irradiance slope
R_0	SENSOR_R0	Sensor resistance in dark conditions
α	RBASE_ALPHA	Semiconductor base resistance parameter
β	RBASE_BETA	Semiconductor base resistance parameter
A	GAS_GAIN	Gas gain
T_0	GAS_T_IRR_OF	Gas τ_1 dependence with light (offset)
T_M	GAS_T_IRR_M	Gas τ_1 dependence with light (slope)
T_2	GAS_T2	Gas second time constant
T_{Onoff}	GAS_R_ONOFF	Gas increasing/decreasing ratio
S_M	SENS_IRRS	Irradiance slope of maximum response as function of gas concentration
S_0	SENS_IRRO	Irradiance offset of maximum response as function of gas concentration
σ	SENS_STD	Standard deviation of the bell-shaped response
C_D	DRIFT_COEF	Drift coefficient

to parts per million (ppm), with electrical power requirements as low as 30 μW.

The experimental data from the sensor were obtained by introducing it into a gas-tight chamber and blending gases by means of a set of mass flow controllers (MFCs, Brondkhorst) flowing at a constant rate of 400 mL/min. The reference atmospheres were produced by diluting certified gas patterns with dry synthetic air (SA) (20% O_2 + 80% N_2 in volume ratio, with a purity of 99.999%, $H_2O < 5$ ppm, and $C_nH_m < 1$ ppm). Patterns of 10 ppm of NO_2, 100 ppm of NH_3, 100 ppm of CO, and 1% of CH_4 were used to incorporate the target gases. The gas chamber was equipped with feedthrough electrical connections to drive the LEDs and to measure the electrical resistance of the SMO layer, using a Keithley 2400 source-meter unit (SMU). LED driving and resistance measurements were carried out under constant current and light irradiance conditions ranging from 25 ppb to 1 ppm.

B. Extraction of Model Parameters

Setting up realistic parameters to run the model can be achieved from a set of reference experiments in four steps. To understand each step, we illustrate the process using the experimental data from the gas sensor described [38] (Fig. 6).

Step (i): The light source parameters are extracted from the characteristic curves of the LED. The reverse saturation current (I_S) and the ideality factor (n) are found by fitting an exponential law to the $I(V)$ curve of the LED. The parasitic components (R_S, R_P, and C_P) needed a more careful characterization of the device, through, e.g., impedance spectroscopy. Another option could be to directly feed the LED current into the model, avoiding the calculation of this voltage-to-current conversion. The irradiance parameters (E_{e0}, E_{eM}, T_{IRR}, and G_{IRR}) are also configured at this stage to set the optical excitation level of the SMO and are found by looking at the sensor response curves under different light intensities.

Step (ii): The parameters defining the sensor steady state (α, β, A_{On}, A_{Off}, and r) are measured during the sensor characterization under constant gas concentration. Here, the sensor "reference" resistance (R_0) is found by keeping the sensor under an arbitrarily chosen "reference" irradiance conditions and in clean air. The response is found after exhaustive measurements of the sensor resistance under the desired light and gas conditions [Fig. 6(a) shows an example of one these measurements], in relation to their value in clean air. Fig. 6(b) shows a summary of responses that clearly display the above-mentioned with the bell-shape trend (from which the σ value can be extracted). Fig. 6(c) gives the relationship between the irradiance and the height of the bell to extract S_0 and S_M.

Step (iii): Out of the same measurements [exemplified in Fig. 6(a)], one can identify the long-term drift effects (C_D) by looking at the slow deviation of the senor signal, not following the overall trend due to the external inputs. In this example, a drift term linear over time was enough to capture the data behavior.

Step (iv): The dynamic parameters (T_0, T_M, T_2, and T_{OnOff}) were taken again from the same experiments [Fig. 6(a)], but now observing the transient behavior of the sensor after each sudden change of the experimental conditions (i.e., gas concentration and/or light irradiance). Fig. 6(d) shows the dependence of the transient times with the gas concentration and the irradiance.

IV. RESULTS

A. Single Irradiance Experiment

After gathering all parameters from the sensor curves, our model can predict quantitatively the resistance measured by the sensor over time (Fig. 7). It follows properly the resistance variations both under a sequence of slow gas pulses (timescale of hours) and under a fast-pulsing illumination background (timescale of seconds). This demonstrates the ability of the tool to predict both the magnitude and the dynamic response of a sensor to varying gas-light environments. Still, the deviations observed reveal operation conditions where the simplifications made in the model start to fail (for example, due to response saturation effects at high gas concentrations). The same experiment modeling illustrates how a linear drift term is a good enough approximation in this particular case.

B. Multiple Irradiance Experiments

The model can also be applied to predict the experimental trends in more complex scenarios, such as comparing the response under widely varying illumination conditions. The same four-step process was used to obtain the parameters needed.

For *Step (i)*, we measured the sensor base resistance as a function of the incident light irradiance. To that end, the device was exposed to light pulses of different intensities with

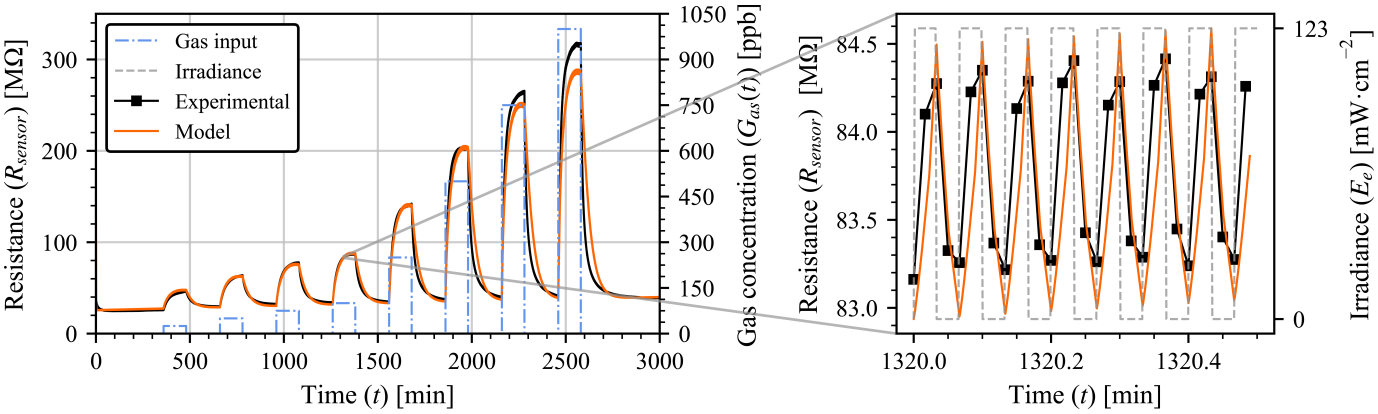

Fig. 7. Model results compared with experimental data from a UV illuminated gas sensor. Left: curve showing the overall transient response to the gas pulses. Right: zoom into the transient details of the model showing the precise response to the light pulses.

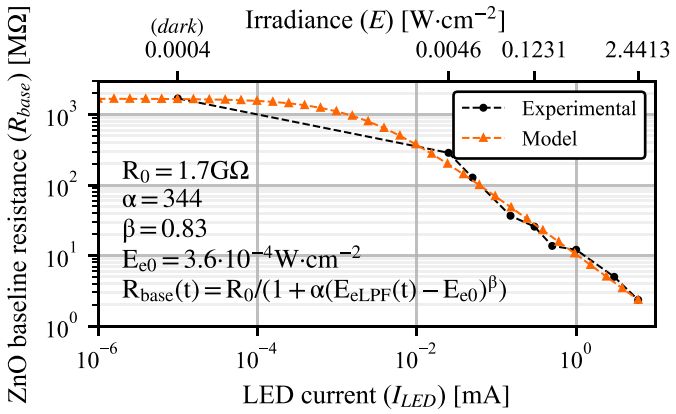

Fig. 8. Baseline resistance model fit for multiple illumination levels.

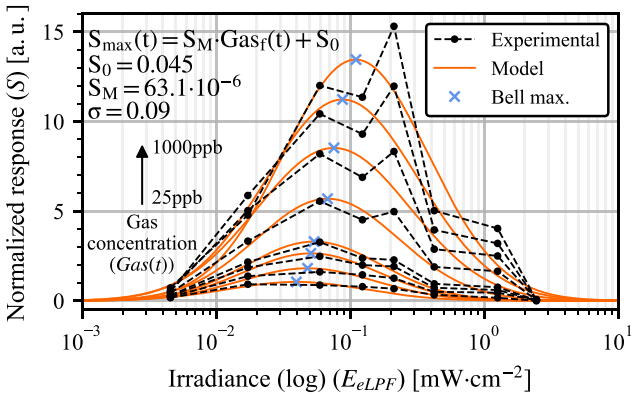

Fig. 9. Gas sensor response model fit for multiple illumination levels and gas concentrations.

a period of 4 s and a duty cycle of 50%. Fig. 8 shows the data of this experiment and its fitting to the model curve of (4). It is worth noting that, in this case, we will refer as the resistance in dark conditions (R_0) to the response of the sensor with an LED current of 10 nA, which is around 1.7 GΩ.

For *Step (ii)*, we measured the resistance variation in response to different gas concentrations now under varying irradiance levels (Fig. 9). Data from the sensor response were again modeled with a bell-shaped curve, following the variations for multiple irradiance and gas concentrations levels. The cross points denote the maximum height of the bell that follow the linear relationship of (12). We observed a certain deviation of the data points from the ideal bell-shaped law, may be because the sensor response also degrades over time. Anyhow, for the sake of the phenomenological model presented, the overall trend is captured. It should be noted that the model takes the standard deviation of the bells as a constant, and this assumption is another approximation taken for simplicity and to keep the code computationally light.

For clarity in *Step (iii)*, we decided to remove the drift term by subtracting the baseline resistance from the data.

In *Step (iv)*, we again collected the transient times of the data collected for both the gas and light variations.

With this new set of model parameters, we simulated the experimental trends presented in Fig. 10. The hashed bands around the model line illustrate the 95% confidence interval of the predictions. This interval was obtained by carrying

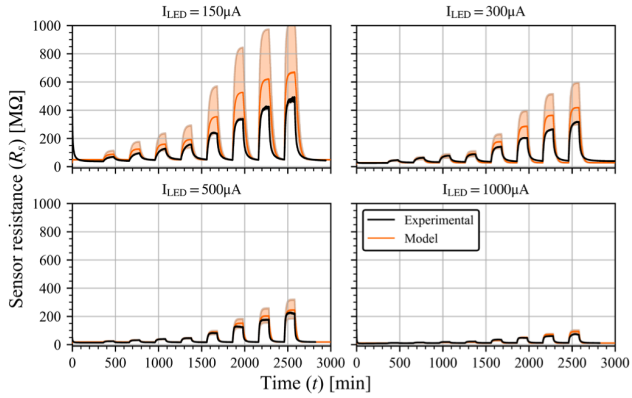

Fig. 10. Photoactivated ZnO gas sensor model behavior for different LED currents. The shadows zones of the model curves represent the sensor variations accounted by the model.

out Monte Carlo simulations in which the model parameters were randomly varied following a normal distribution around their central values with a span of two times their standard deviation.

As can be seen, the model follows accurately the sensor behavior for the higher LED currents with all the points within the model confidence interval. Deviations are tough larger for lower LED currents (low irradiance), but are enough to identify the worst case operation points, allowing a designer to simulate the front-end electronics working along with a sensor.

V. Conclusion

We presented a Verilog-A model of the electrical behavior of illuminated SMO gas sensors, based on a phenomenological description of the trends observed in this type of sensors, that requires a reduced set of experimental parameters.

The model predicts accurately the variations in sensor resistance once its parameters have been approximated to experimental estimates. The model can deal with the uncertainty in these parameters by means of Monte Carlo methods.

The accuracy of the model is enough to predict qualitative trends and get quantitative estimation of the resistance values. Despite the deviations observed in some cases, static and dynamic values are good enough to identify the design conditions for the design, simulation, and optimization of interfacing electronics.

The model is modular and can be improved by incorporating more detailed and/or complex descriptions of the effects involved, such as drift components and response variation with the light wavelength, among others. To facilitate access and reuse by the scientific community, we published the source code in an open GitHub repository [42]. Thus, anyone can use or modify the model for its own purposes, adding new features or improvements.

References

[1] N. Egerstrom et al., "Health and economic benefits of WHO air quality guidelines, western Pacific region," *Bull. World Health Org.*, vol. 101, no. 2, pp. 130–139, Feb. 2023.

[2] W. Tsujita, A. Yoshino, H. Ishida, and T. Moriizumi, "Gas sensor network for air-pollution monitoring," *Sens. Actuators B, Chem.*, vol. 110, no. 2, pp. 304–311, Oct. 2005, doi: 10.1016/j.snb.2005.02.008.

[3] H. Li, Z. Yang, W. Ling, D. Zhu, and Y. Pu, "UV excited gas sensing SnO_2–ZnO aerogels to ppb-level ethanol detection," *Sens. Actuators B, Chem.*, vol. 337, Jun. 2021, Art. no. 129815, doi: 10.1016/j.snb.2021.129815.

[4] P. Kumar et al., "Indoor air quality and energy management through real-time sensing in commercial buildings," *Energy Buildings*, vol. 111, pp. 145–153, Jan. 2016, doi: 10.1016/j.enbuild.2015.11.037.

[5] G. Wiegleb and J. Heitbaum, "Semiconductor gas sensor for detecting NO and CO traces in ambient air of road traffic," *Sens. Actuators B, Chem.*, vol. 17, no. 2, pp. 93–99, Jan. 1994, doi: 10.1016/0925-4005(94)87035-7.

[6] T. Hübert, L. Boon-Brett, V. Palmisano, and M. A. Bader, "Developments in gas sensor technology for hydrogen safety," *Int. J. Hydrogen Energy*, vol. 39, no. 35, pp. 20474–20483, Dec. 2014, doi: 10.1016/j.ijhydene.2014.05.042.

[7] M. Utriainen, E. Kärpänoja, and H. Paakkanen, "Combining miniaturized ion mobility spectrometer and metal oxide gas sensor for the fast detection of toxic chemical vapors," *Sens. Actuators B, Chem.*, vol. 93, nos. 1–3, pp. 17–24, Aug. 2003, doi: 10.1016/s0925-4005(03)00337-x.

[8] J. W. Gardner and P. N. Bartlett, "A brief history of electronic noses," *Sens. Actuators B, Chem.*, vol. 18, nos. 1–3, pp. 210–211, Mar. 1994, doi: 10.1016/0925-4005(94)87085-3.

[9] M. I. A. Asri, M. N. Hasan, M. R. A. Fuaad, Y. M. Yunos, and M. S. M. Ali, "MEMS gas sensors: A review," *IEEE Sensors J.*, vol. 21, no. 17, pp. 18381–18397, Sep. 2021, doi: 10.1109/JSEN.2021.3091854.

[10] J. Luo, X. Feng, H. Kan, H. Li, and C. Fu, "One-dimensional Bi_2S_3 nanobelts-based surface acoustic wave sensor for NO_2 detection at room temperature," *IEEE Sensors J.*, vol. 21, no. 2, pp. 1404–1408, Jan. 2021, doi: 10.1109/JSEN.2020.3020301.

[11] D. López-Torres et al., "Sensitivity optimization of a microstructured optical fiber ammonia gas sensor by means of tuning the thickness of a metal oxide nano-coating," *IEEE Sensors J.*, vol. 19, no. 13, pp. 4982–4991, Jul. 2019, doi: 10.1109/JSEN.2019.2901361.

[12] H. Nazemi, A. Joseph, J. Park, and A. Emadi, "Advanced micro- and nano-gas sensor technology: A review," *Sensors*, vol. 19, no. 6, p. 1285, Mar. 2019, doi: 10.3390/s19061285.

[13] N. Barsan, D. Koziej, and U. Weimar, "Metal oxide-based gas sensor research: How to?" *Sens. Actuators B, Chem.*, vol. 121, no. 1, pp. 18–35, Jan. 2007, doi: 10.1016/j.snb.2006.09.047.

[14] Y. Zheng, L. Wang, H. Tian, L. Qiao, Y. Zeng, and C. Liu, "Bimetal carbonaceous templates for multi-shelled $NiCo_2O_4$ hollow sphere with enhanced xylene detection," *Sens. Actuators B, Chem.*, vol. 339, Jul. 2021, Art. no. 129862, doi: 10.1016/j.snb.2021.129862.

[15] W. Chen, Z. Wang, S. Gu, and J. Wang, "Detection of hexanal in humid circumstances using hydrophobic molecularly imprinted polymers composite," *Sens. Actuators B, Chem.*, vol. 291, pp. 141–147, Jul. 2019, doi: 10.1016/j.snb.2019.04.065.

[16] M. V. Nikolic, V. Milovanovic, Z. Z. Vasiljevic, and Z. Stamenkovic, "Semiconductor gas sensors: Materials, technology, design, and application," *Sensors*, vol. 20, no. 22, p. 6694, Nov. 02, 2020, doi: 10.3390/s20226694.

[17] Y. Kang, F. Yu, L. Zhang, W. Wang, L. Chen, and Y. Li, "Review of ZnO-based nanomaterials in gas sensors," *Solid State Ionics*, vol. 360, Feb. 2021, Art. no. 115544, doi: 10.1016/j.ssi.2020.115544.

[18] A. Moumen, G. C. W. Kumarage, and E. Comini, "P-type metal oxide semiconductor thin films: Synthesis and chemical sensor applications," *Sensors*, vol. 22, no. 4, p. 1359, Feb. 01, 2022, doi: 10.3390/s22041359.

[19] D. E. Williams, "Semiconducting oxides as gas-sensitive resistors," *Sens. Actuators B, Chem.*, vol. 57, nos. 1–3, pp. 1–16, Sep. 1999, doi: 10.1016/s0925-4005(99)00133-1.

[20] H. Wang et al., "Gas sensing materials roadmap," *J. Phys., Condens. Matter*, vol. 33, no. 30, Jul. 01, 2021, Art. no. 303001, doi: 10.1088/1361-648x/abf477.

[21] A. Dey, "Semiconductor metal oxide gas sensors: A review," *Mater. Sci. Eng., B*, vol. 229, pp. 206–217, Mar. 2018, doi: 10.1016/j.mseb.2017.12.036.

[22] T. Li, L. Xu, and Y. Wang, "Micro-heater-based gas sensors," in *Micro Electro Mechanical Systems* (Micro/Nano Technologies), Q. A. Huang, Ed. Singapore: Springer, 2018, doi: 10.1007/978-981-10-5945-2_21.

[23] C. Fàbrega, O. Casals, F. Hernández-Ramírez, and J. D. Prades, "A review on efficient self-heating in nanowire sensors: Prospects for very-low power devices," *Sens. Actuators B, Chem.*, vol. 256, pp. 797–811, Mar. 2018, doi: 10.1016/j.snb.2017.10.003.

[24] E. Comini, G. Faglia, and G. Sberveglieri, "UV light activation of tin oxide thin films for NO_2 sensing at low temperatures," *Sens. Actuators B, Chem.*, vol. 78, nos. 1–3, pp. 73–77, Aug. 2001, doi: 10.1016/s0925-4005(01)00796-1.

[25] N. Barsan and U. Weimar, "Conduction model of metal oxide gas sensors," *J. Electroceram.*, vol. 7, pp. 143–167, Dec. 2001, doi: 10.1023/A:1014405811371.

[26] W. Göpel and K. D. Schierbaum, "SnO_2 sensors: Current status and future prospects," *Sens. Actuators B, Chem.*, vol. 26, nos. 1–3, pp. 1–12, Jan. 1995, doi: 10.1016/0925-4005(94)01546-t.

[27] W. Li et al., "UV light irradiation enhanced gas sensor selectivity of NO_2 and SO_2 using rGO functionalized with hollow SnO_2 nanofibers," *Sens. Actuators B, Chem.*, vol. 290, pp. 443–452, Jul. 2019, doi: 10.1016/j.snb.2019.03.133.

[28] T. Ueda, M. M. H. Bhuiyan, H. Norimatsu, S. Katsuki, T. Ikegami, and F. Mitsugi, "Development of carbon nanotube-based gas sensors for NOx gas detection working at low temperature," *Phys. E, Low-Dimensional Syst. Nanostruct.*, vol. 40, no. 7, pp. 2272–2277, May 2008, doi: 10.1016/j.physe.2007.12.006.

[29] O. Monereo et al., "Carbon nanofiber flexible gas sensor modulated by UV light," in *Proc. 17th Int. Conf. Solid-State Sensors, Actuators Microsyst.*, Jun. 2013, pp. 1154–1157, doi: 10.1109/Transducers.2013.6626977.

[30] C.-M. Yang, T.-C. Chen, Y.-C. Yang, M.-C. Hsiao, M. Meyyappan, and C.-S. Lai, "Ultraviolet illumination effect on monolayer graphene-based resistive sensor for acetone detection," *Vacuum*, vol. 140, pp. 89–95, Jun. 2017, doi: 10.1016/j.vacuum.2016.08.006.

[31] L. F. da Silva et al., "UV-enhanced ozone gas sensing response of ZnO–SnO_2 heterojunctions at room temperature," *Sens. Actuators B, Chem.*, vol. 240, pp. 573–579, Mar. 2017, doi: 10.1016/j.snb.2016.08.158.

[32] M. Reddeppa et al., "H_2, H_2S gas sensing properties of rGO/GaN nanorods at room temperature: Effect of UV illumination," *Sens. Actuators B, Chem.*, vol. 264, pp. 353–362, Jul. 2018, doi: 10.1016/j.snb.2018.03.018.

[33] J. D. Prades et al., "A model for the response towards oxidizing gases of photoactivated sensors based on individual SnO_2 nanowires," *Phys. Chem. Chem. Phys.*, vol. 11, no. 46, p. 10881, 2009, doi: 10.1039/b915646a.

[34] E. Espid and F. Taghipour, "UV-LED photo-activated chemical gas sensors: A review," *Crit. Rev. Solid State Mater. Sci.*, vol. 42, no. 5, pp. 416–432, Sep. 2017, doi: 10.1080/10408436.2016.1226161.
[35] J. D. Prades et al., "Equivalence between thermal and room temperature UV light-modulated responses of gas sensors based on individual SnO_2 nanowires," *Sens. Actuators B, Chem.*, vol. 140, no. 2, pp. 337–341, Jul. 2009, doi: 10.1016/j.snb.2009.04.070.
[36] *Verilog-AMS Language Reference Manual*, Accellera Syst. Initiative Inc., Napa, CA, USA, 2014.
[37] N. Markiewicz et al., "Micro light plates for low-power photoactivated (gas) sensors," *Appl. Phys. Lett.*, vol. 114, no. 5, Feb. 2019, Art. no. 053508, doi: 10.1063/1.5078497.
[38] O. Casals et al., "A parts per billion (PPB) sensor for NO_2 with microwatt (μW) power requirements based on micro light plates," *ACS Sensors*, vol. 4, no. 4, pp. 822–826, Apr. 2019, doi: 10.1021/acssensors.9b00150.
[39] S. King, "Luminous intensity of an LED as a function of input power," *Int. School Bangkok J. Phys.*, vol. 2, pp. 1–4, Jun. 2008.
[40] F. Ménil, M. Susbielles, H. Debéda, C. Lucat, and P. Tardy, "Evidence of a correlation between the non-linearity of chemical sensors and the asymmetry of their response and recovery curves," *Sens. Actuators B, Chem.*, vol. 106, no. 1, pp. 407–423, Apr. 2005, doi: 10.1016/j.snb.2004.08.027.
[41] S. Di and M. Falasconi, "Drift correction methods for gas chemical sensors in artificial olfaction systems: Techniques and challenges," in *Advances in Chemical Sensors*. Rijeka, Croatia: InTech, Jan. 2012, doi: 10.5772/33411.
[42] *Model GitHub Repository*. Accessed: Feb. 26, 2024. [Online]. Available: https://github.com/jlusoler/gas_sensor_model/tree/main

Juan Luis Soler-Fernández received the B.E. degree in electronics and telecommunications engineering from the University of Barcelona, Barcelona, Spain, in 2020, and the M.S. degree in microelectronics from the University of Seville, Seville, Spain, in 2023. He is currently pursuing the Ph.D. degree in engineering and applied science with the VLSI Design Group, Department of Electronics and Biomedical Engineering, University of Barcelona.

His research interests include VLSI design for low-power applications.

Olga Casals graduated in optics and optometry from the Faculty of Optics and Optometry of Terrassa (FOOT), Polytechnic University of Catalonia, Barcelona, Spain, in 1994. She graduated in physics from the University of Barcelona, Barcelona, in 2001, and the doctor degree from the Department of Electronics, University of Barcelona in 2012.

She is currently working with the University of Barcelona. She is also an Optic and Optometrist with Universitat Politècnica de Catalunya (UPC), Barcelona, and a physicist. After working with the Research and Development Department, TECIL S.A., Barcelona, she returned to UB to hold different postdoctoral fellowships, including TecnioSpring with a stay in Technical University of Braunschweig, Braunschweig, Germany.

Cristian Fàbrega received the bachelor's degree in physics, the master's degree in nanoscience and nanotechnology, and the Ph.D. degree in nanoscience from the Universitat de Barcelona, Barcelona, Spain.

He is currently an Associate Professor with the Department of Electronics and Biomedical Engineering, University of Barcelona. His research interests are centered in the development of novel device concepts based on light–matter interaction with better and improved performance, paying special attention to the integration and power consumption. He is also intensively involved in the fabrication, characterization, and integration of functional devices for environmental applications (e.g., gas sensors and solar-to-gas), based on material interfaces and charge separation mechanisms.

Hongqiang Li received the B.E., M.Sc., and Ph.D. degrees from Tianjin Polytechnic University, China.

He is currently a Professor with the School of Electronics and Information Engineering, Tianjin Polytechnic University, China, and performs research activity at the Tianjin Key Laboratory of Optoelectronic Detection Technology and Systems. His current research interests include fibre Bragg grating sensors, interrogation system, and silicon-based photonic integration. The main goal of his research is build a low-cost monolithic integration of fibre Bragg grating interrogation system on a silicon wafer.

Angel Diéguez was born in Barcelona, Spain, in 1970. He received the graduate and doctorate degrees in physics from the University of Barcelona, Barcelona, in 1993 and 1999, respectively.

Since 2001, he has been a Professor with the Department of Electronics and Biomedical Engineering, University of Barcelona, where he carried out research in VLSI circuits and systems in biomedical, instrumentation, and high-energy physics. In 2013, he cofounded endoASIC Technologies, Barcelona, a spin-off company of the University of Barcelona dedicated to the development of capsule endoscopy technology and molecular in vitro and in vivo diagnosis. He has coauthored more than 100 articles in international peer-reviewed journals and has contributed to more than 200 conferences. During his time at the University of Barcelona, he has supervised seven Ph.D. degree students on VLSI design and 36 master's and graduate projects. He has participated in eight European projects and 18 national projects. He has been the coordinator of several international and national research projects involving high-energy physics, SPAD CMOS sensors, CMOS circuits for robotics, or CMOS sensors and drivers for microscopy. He has coauthored five patents.

J. Daniel Prades received the Ph.D. degree in nanoscience with the Universitat de Barcelona, Barcelona, Spain.

He has been a Full Professor at the Universitat de Barcelona since 2019 and leads his group on gas and optical sensors. He is currently a Physicist and an Electronic Engineer with Universitat de Barcelona. In 2024, he was appointed as an Alexander von Humboldt Professor at the Technical University of Braunschweig, Braunschweig, Germany, to develop a new research line on "ubiquitous metrology" or how sensor data can be made more accurate, reliable, and traceable.

Oscar Alonso was born in Barcelona in 1982. He received the Ph.D. degree in engineering and advanced technologies from the University of Barcelona, Barcelona, Spain, in 2012.

He is currently an Associate Professor with the University of Barcelona. His research interests include VLSI circuit design. He has designed ASICs for different applications, among which there are design of analog IPs for present and future trackers for high-energy colliders (Belle II tracker in Japan, ILC), design of IPs for RISC-V-based cores, development of novel medical and biomedical devices, and design of system on chips (SoC) for sustainable and autonomous applications [for example, the Internet of Things (IoT)].